Energy & Environmental Science

PAPER

Optimized thermoelectric properties of $Mo_3Sb_{7-x}Te_x$ with significant phonon scattering by electrons

Xiaoya Shi,[a] Yanzhong Pei,[b] G. Jeffrey Snyder[b] and Lidong Chen*[a]

Heavily doped compounds $Mo_3Sb_{7-x}Te_x$ ($x = 0$, 1.0, 1.4, 1.8) were synthesized by solid state reaction and sintered by spark plasma sintering. Both X-ray diffraction and electron probe microanalysis indicated the maximum solubility of Te was around $x = 1.8$. The trends in the electrical transport properties can generally be understood using a single parabolic band model, which predicts that the extremely high carrier concentration of Mo_3Sb_7 ($\sim 10^{22}$ cm^{-3}) can be reduced to a nearly optimized level ($\sim 2 \times 10^{21}$ cm^{-3}) for thermoelectric figure of merit (zT) by Te-substitution with $x = 1.8$. The increased lattice thermal conductivity by Te-doping was found to be due to the decreased Umklapp and electron–phonon scattering, according to a Debye model fitting. The thermoelectric figure of merit (zT) monotonously increased with increasing temperature and reached its highest value of about 0.51 at 850 K for the sample with $x = 1.8$, making these materials competitive with the state-of-the-art thermoelectric SiGe alloys. Evidence of significant electron–phonon scattering is found in the thermal conductivity.

1. Introduction

Thermoelectrics (TE) provides a new approach to save energy. Both the power generations utilizing the Seebeck effect and the cooling applications utilizing the Peltier effect attract more and more attention.[1–5] The ideal TE materials should have a large Seebeck coefficient, S, and high electrical conductivity, σ, as well as low thermal conductivity, κ. The TE materials are evaluated by comparing the figure of merit zT, defined as $zT = (S^2\sigma/\kappa)T$.[6] Usually, reducing the thermal conductivity is one of the best

ways to strive for a high zT. During the last decade, nano-structured materials have been introduced and proved to be effective for decreasing thermal conductivity, leading to break-throughs in zT.[7–9] On the other hand, it is believed that heavily doped semiconductors, especially those composed of complex structures and heavy elements, are likely candidates for TE applications.[1] This is because relatively low thermal conductivity can be realized in complex systems with large unit cells containing heavy elements.[10,11] Successful examples of new thermo-electric materials such as $La_{3-x}Te_4$ and $Yb_{14}MnSb_{11}$,[12–15] have been hotly studied for high-temperature TE application during the past decade.

Some of the recent reports indicate that the Mo_3Sb_7 based compounds, crystallizing in the complex cubic Ir_3Ge_7 structure type, also show great potential for high temperature TE applications.[16–21] The matrix compound Mo_3Sb_7 exhibits strong

[a]*CAS Key laboratory of Materials for Energy Conversion, Shanghai Institute of Ceramics, Chinese Academy of Science, 1295 Dingxi Road, Shanghai, 200050, PR China. E-mail: chenlidong@mail.sic.ac.cn; Fax: +86-21-52413122; Tel: +86-21-52412522*
[b]*Materials Science, California Institute of Technology, Pasadena, CA, 91125, USA*

Broader context

Thermoelectric materials have attracted significant interest worldwide because they can directly convert thermal energy to electrical energy. Nowadays more and more effort is focused on the exploration of new compounds with non-toxic and Earth-abundant elements. Mo_3Sb_7 is one of the most promising and inexpensive thermoelectric materials. It is effective to optimize the carrier concentration in this "poor metal" by substituting tellurium on the antimony site. The limit of Te/Sb substitution fraction is around 1.8/7.0, which is near the maximum point of the power factor calculated with the single parabolic band model. It is interesting to observe the phonon scattering by the electrons in this "poor metal" by modeling the experimental data using the Debye model, which helps understand the increased lattice thermal conductivity due to the decreased carrier concentration after Te/Sb doping. The predicted zT peak locates at the lower carrier concentration region as compared with the power factor, which indicates further improvement in the thermoelectric performance of Mo_3Sb_7 should be expected through doping on the Mo site.

4086 | *Energy Environ. Sci.*, 2011, **4**, 4086–4095

This journal is © The Royal Society of Chemistry 2011

p-type metallic behavior because the Fermi level locates deep into the valence band. The effective way to optimize the electrical performance is to move the Fermi level towards the valence band maximum, which means more electrons are needed for this compound. Theoretical calculations showed that partial substitution of Sb by Te elements would effectively shift the Fermi levels and then optimize the TE performance, which was confirmed by the experiments.[18,22–25] High zT value of 0.8 at 1050 K was reported, making this material an outstanding candidate for high-temperature TE power generation.[18]

However, it is not clear if higher performance would be achieved if the carrier concentration could be further reduced. Attempts to reduce both the carrier concentration and the lattice thermal conductivity by filling with 3-d transition metals has shown to be largely unsuccessful.[22,23] Relatively accurate predictions might be accomplished with a thorough investigation of the transport properties in $Mo_3Sb_{7-x}Te_x$ compounds especially the high-temperature carrier scattering mechanism, combined with a model of the band structure, such as a single parabolic band model.[26] Moreover, for the thermal transport, the reason for the increased high-temperature lattice thermal conductivity after Te-doping is still unclear.

In this paper, the electrical properties, including the carrier scattering mechanism, were carefully studied. By introducing the single parabolic band model, the optimal carrier concentration and doping level could be predicted for the Te-doped system that should also be applicable to other dopant systems. Using the Debye model we find an abnormal lattice thermal conductivity behavior with Te doping, resulting in a softening of the phonons (increased Debye temperature), but also a reduction in the electron–phonon scattering as the carrier concentration is reduced.

2. Experimental details

High-purity elements Mo (99.5%, powder), Sb (99.999%, powder) and Te (99.999%, powder) were used as the starting materials. The powders were first prepared in the molar ratio of Mo : Sb : Te = 3 : 7-x : x. Subsequently, they were synthesized by a direct solid state reaction method at 1073 K in evacuated silica tubes. The mixture was kept at this temperature for 7 days followed by another 7 days' annealing at 923 K. Finally the products were ground into fine powder and sintered using spark plasma sintering (SPS 2040, Simitomo) between 900 and 950 K for 5 min under 60 MPa uniaxial pressure. The relative densities of the samples (see Table I) are all over 97%.

The phase composition of the samples was determined by powder X-ray diffraction (XRD), which was carried out on a Rigaku 69 D/max2250 diffractometer (Cu-Kα radiation,

$\lambda = 0.15418$ nm, 40 kV/200 mA) and the compositional homogeneity of all the samples was examined by electron probe microanalysis (EPMA, JEOL, JXA-8100). The thermal and electrical properties were divided into two parts. Low temperature (2 K to room temperature) data were collected from the Physical Property Measurement System (PPMS, Quantum Design). For the high temperature (room temperature to 850 K) part, thermal conductivity was first measured by a laser flash technique (NETZSCH LFA427). Then the samples were cut into about 1.5 ×1.5 ×10 mm sized bars for electrical property measurements. Electrical conductivity (σ) was measured using a standard four-probe method. The Seebeck coefficient (S) was determined from the slope of the thermoelectromotive (ΔE) force versus the temperature gradient (0 < ΔT < 4 K). All these high temperature transport measurements were carried out under flowing Ar atmosphere.

3. Results and discussion

Electrical properties

Fig. 1 shows the XRD patterns for $Mo_3Sb_{7-x}Te_x$ ($0 \leq x \leq 2.2$). The result shows that all samples are single phases when x is less than or equal to 1.8. However, the second phase of $MoTe_2$ could be obtained when the Te content is higher than 1.8. This could be further confirmed from the EPMA results. The lattice parameters of the samples, as shown in Fig. 2, were calculated from the high-angle XRD data. Due to the smaller atomic radius of Te element compared with Sb, the lattice parameter decreases almost linearly with increasing the Te doping fraction for single phased samples. However, when the Te content exceeds $x = 1.8$ the lattice parameter becomes a constant (shown in Fig. 2). The
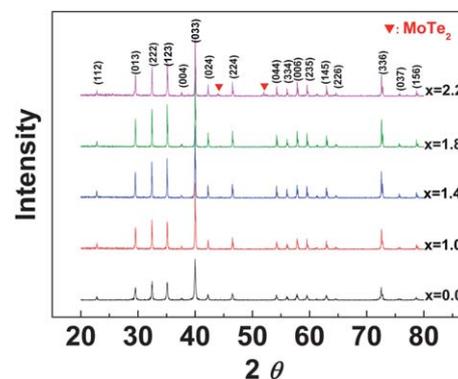

Fig. 1 Powder X-ray diffraction patterns for $Mo_3Sb_{7-x}Te_x$ The symbols ▼ show the peaks of the second phase $MoTe_2$ and the other marked peaks represent the Mo_3Sb_7 phase.

Table 1 Room temperature properties of the nominal composition, EPMA composition, relative density and lattice parameter for $Mo_3Sb_{7-x}Te_x$

Nominal composition	EPMA composition	Relative density ρ (%)	Lattice parameter a/Å
Mo_3Sb_7	$Mo_3Sb_{7.01}$	98.7	9.57125
Mo_3Sb_6Te	$Mo_3Sb_{6.05}Te_{0.96}$	97.5	9.5673
$Mo_3Sb_{5.6}Te_{1.4}$	$Mo_3Sb_{5.66}Te_{1.38}$	98.0	9.56616
$Mo_3Sb_{5.2}Te_{1.8}$	$Mo_3Sb_{5.25}Te_{1.76}$	98.6	9.56544
$Mo_3Sb_{4.8}Te_{2.2}$	$Mo_3Sb_{5.28}Te_{1.75}$	97.0	9.56562

This journal is © The Royal Society of Chemistry 2011

Energy Environ. Sci., 2011, **4**, 4086–4095 | 4087

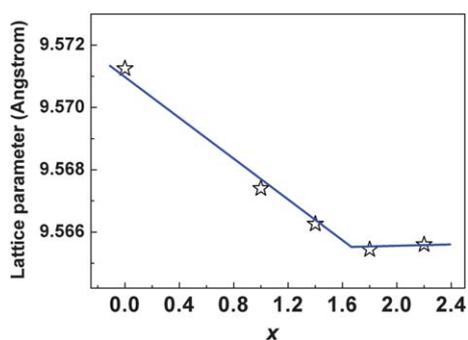**Fig. 2** The lattice parameters of $Mo_3Sb_{7-x}Te_x$ as a function of the doping fraction x. The solid line is the trend of the data.

EPMA composition data in Table 1, reveal that the actual chemical compositions of $x = 1.8$ and $x = 2.2$ (main phase) samples are very close. Therefore, these results indicate that the solubility for Te/Sb substitution is limited to around 1.8/7.0, consistent with previous reports.[23]

Fig. 3 exhibits the high temperature electrical properties of $Mo_3Sb_{7-x}Te_x$. All samples show metallic conducting behavior with a positive Seebeck coefficient within the whole temperature range. The parent compound Mo_3Sb_7 possesses extremely high electrical conductivity (6.2×10^5 Sm^{-1}) and a small Seebeck coefficient (17 μVK^{-1}) at room temperature, which indicates that the Fermi level locates deep into the valence band. As a result, the power factor ($PF = S^2\sigma$) of this sample is small, even at high temperature. As expected, Te could act as an effective donor and improves the electrical performance by adding more electrons (reducing holes) in the system. The power factor is enhanced, especially at high temperature, increasing from 10.5×10^{-4} W m^{-1} K^{-2} for the parent compound to 19.3×10^{-4} W m^{-1} K^{-2} for $x = 1.8$ at 850 K. The room temperature electrical conductivity and the Seebeck coefficient data are shown in

Fig. 3d. Electrical conductivity decreases while the Seebeck coefficient increases with increasing the doping fraction when $x \leq 1.8$. However, the sample with nominal $x = 2.2$ does not follow the same trend. The deviation of the property can be attributed to the existence of second phase $MoTe_2$, as mentioned above.

For clarity, the low-temperature electrical properties (measured from PPMS) were plotted separately in Fig. 4. The data exhibit very good coincidence with those obtained from high-temperature measurement (within 10% disagreement at room temperature). Fig. 5 shows the temperature dependence of hole concentration p_H obtained from the formula $p_H \cdot e = 1/R_H$ (assuming only one type carrier) by measuring the Hall coefficient R_H, here e is the electronic charge. The temperature-independent (above 50 K) hole concentration is obtained, which again suggests heavily doped metallic behavior. The hole concentration diminishes with increasing x, which is the main reason for the decrease of electrical conductivity. All these results agree well with those reported previously.[24,25]

In order to determine the carrier scattering process, the Hall mobility μ_H, defined as $\mu_H = R_H \cdot \sigma$, was calculated using the low-temperature electrical conductivity σ(Fig. 4a) and the Hall coefficient R_H. The temperature dependence of the Hall mobility is plotted in Fig. 6. For comparison, the data from ref. 24 are also exhibited in Fig. 6. Besides the nearly constant Hall mobility below 100 K, all samples show decreased Hall mobility with increasing the temperature (above 100 K). The Hall mobility of all the samples follows the relationship around $\mu_H \sim T^{-0.5}$ near the room temperature range. The data from ref. 24 also contain the $\mu_H \sim T^{-0.5}$ relationship instead of $\mu_H \sim T^{-1.5}$ as described by the authors, which is plotted for comparison in Fig. 6. In order to further investigate the scattering mechanism, the high temperature relationship was also studied using the van der Pauw technique with a 2 T field and pressure-assisted contacts. Experimental data of the Hall coefficient from the sample $x = 1.8$, which was displayed in Fig. 7, shows that the
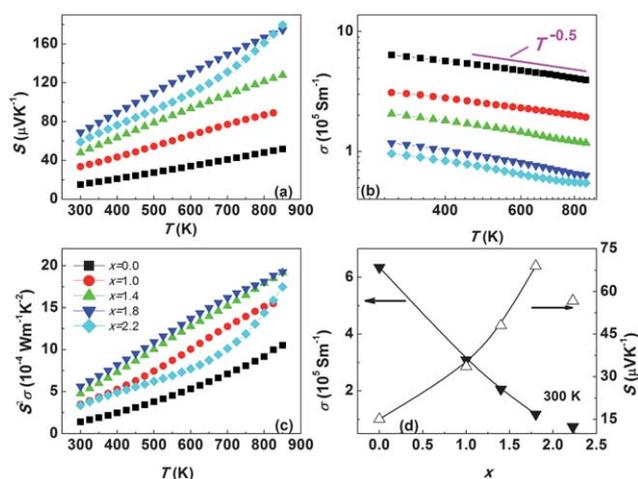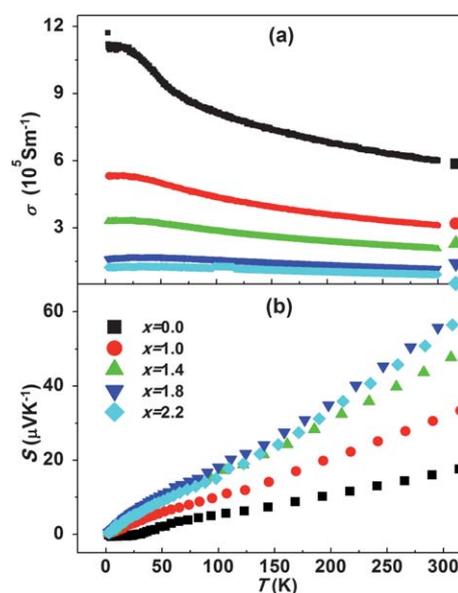

Fig. 3 Temperature dependence of the Seebeck coefficient (a), the electrical conductivity (b) and the power factor (c) for $Mo_3Sb_{7-x}Te_x$. Fig. 3d plots the electrical conductivity and Seebeck coefficient of $Mo_3Sb_{7-x}Te_x$ as a function of x at room temperature. Section (b) shows the $T^{-0.5}$ temperature dependence of electrical conductivity.

Fig. 4 Temperature dependence of electrical conductivity (a) and Seebeck coefficient (b) for $Mo_3Sb_{7-x}Te_x$ from 2 to 300 K.
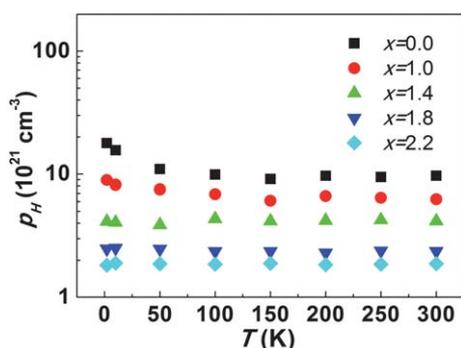
Fig. 5 Temperature dependence of the hole concentration for $Mo_3Sb_{7-x}Te_x$ from 2 to 300 K.

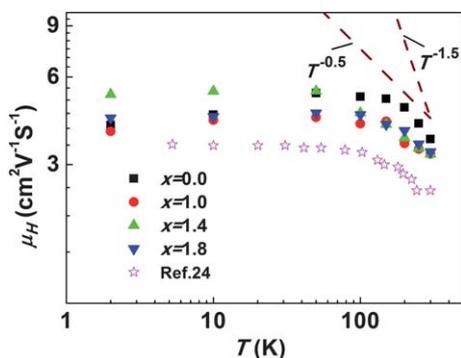**Fig. 6** Temperature dependence of the Hall mobility for $Mo_3Sb_{7-x}Te_x$ from 2 to 300 K. The dashed lines stand for the $T^{-0.5}$ and $T^{-1.5}$ relationship, respectively. The points marked with ☆ represent the data from ref. 24.
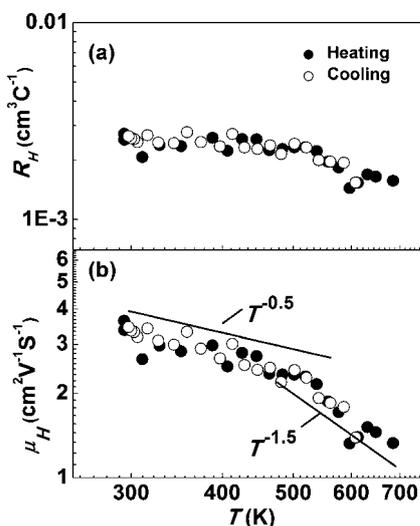

Fig. 7 The temperature dependence of the Hall coefficient for sample $x = 1.8$ from 300 to 700 K during heating and cooling processes. The solid lines represent the $T^{-0.5}$ and $T^{-1.5}$ relationship, respectively.

high-temperature Hall coefficient is still or nearly a constant with only a slight decrease after 500 K. The Hall mobility data in Fig. 7b show the relationship follows $\mu_H \sim T^{-0.5}$ below 500 K, consistent with that found in Fig. 6. Furthermore, electrical

conductivity in Fig. 3b also shows a nearly similar temperature dependence ($\sigma \sim T^{-0.5}$) for the entire temperature range. If it is assumed that the carrier concentration is temperature independent, this relationship can be considered as the temperature dependence of the Hall mobility, according to the formula

$$\sigma = p_H \cdot e \cdot \mu_H \tag{1}$$

As a result, all the samples should exhibit a nearly $\mu_H \sim T^{-0.5}$ relationship, which is typical alloying scattering behavior. As for the decrease of the Hall coefficient and the Hall mobility above 500 K in Fig.7, it may be attributed to the minority carriers. Moreover, the acoustic phonon scattering mechanism should also exist in this semiconductor, especially at high temperature. The mobility and electrical conductivity have faster decay with temperature for acoustic phonon scattering with the expected relationship between $\mu_H \sim T^{-1.0}$ (degenerate) and $\mu_H \sim T^{-1.5}$ (non-degenerate) which may explain the faster decrease of electrical conductivity at high temperature in Fig. 3b. Thus the electrical performance of the Te-doped Mo_3Sb_7 system is likely determined by the multiple scattering mechanisms of alloying scattering and acoustic phonon scattering.

According to the Boltzmann transport equations (within the single parabolic band assumption), the Seebeck coefficient S and the hole concentration p_H are given by

$$S = -\frac{k_B}{e}\left(\frac{(2+\lambda)F_{\lambda+1}(\eta)}{(1+\lambda)F_\lambda(\eta)} - \eta\right), \tag{2}$$

$$p_H = \frac{4\pi(2m*k_BT)^{3/2}}{h^3}F_{1/2}(\eta). \tag{3}$$

with the Fermi integrals $F_j(\eta)$ defined by

$$F_j(\eta) = \int_0^\infty \frac{\xi^j d\xi}{1+\exp(\xi-\eta)}. \tag{4}$$

Here, ξ is the reduced carrier energy, $\eta = E_F/k_BT$ is the reduced electrochemical potential, and λ relates to the energy dependence of the carrier relaxation time, τ, such that $\tau = \tau_0 \cdot \varepsilon^{\lambda-1/2}$ where the expression for τ_0 depends on λ. k_B, e, h and $m*$ are the Boltzmann constant, the elementary charge, the Planck constant and the effective mass, respectively. Considering the alloying scattering and the acoustic phonon scattering give the same λ value, which is $\lambda = 0$, eqn (2) can be simplified to

$$S = -\frac{k_B}{e}\left(\frac{2F_1(\eta)}{F_0(\eta)} - \eta\right). \tag{5}$$

From eqn (3) and (5) we can obtain the $S \sim p_H$ relationship under the single parabolic band model (SPB). As shown in Fig. 8, the hole concentration dependence of the Seebeck coefficient follows the SPB line well at room temperature. Furthermore, the data from ref. 24 also locate around the line. In other words, the single parabolic model seems to be reasonable and suitable for all but perhaps the highest carrier concentration sample. The solid line in Fig. 8 is generated using $\lambda = 0$, and an effective mass of $m* = 5.5m_e$ at room temperature, which is consistent with previously reported values.[24] In addition, the high temperature $S \sim p_H$ relationship was assumed and plotted in the insert figure, which also follows the SPB model. Here, considering the nearly
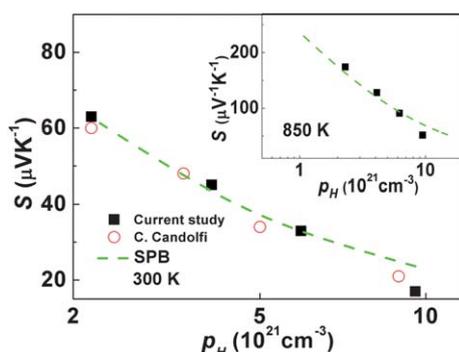
Fig. 8 Carrier concentration dependence of the Seebeck coefficient at 300 and 850 K, respectively. The circled data are from ref. 24 by C. Candolfi, *et al.* The dashed lines represent the theoretical results from the SPB model.

temperature-independent carrier concentration, we used the room temperature hole concentration as high-temperature p_H to make a rough assumption. As a result, with the SPB model, the theoretical high-temperature electrical property PF could be calculated to predict the electrical performance as a function of the carrier concentration. Although the scattering mechanism is complicated in this system, for simplicity, we assume acoustic phonon scattering at high temperatures. Then the PF could be expressed based on the following equations:

$$PF = S^2 \cdot \sigma \qquad (6)$$

$$\mu_H = \frac{\mu_0 \pi^{1/2} F_\lambda(\eta)}{2\Gamma(1+\lambda)F_{1/2}(\eta)} \qquad (7)$$

Here μ_0 is the intrinsic mobility PF and η is finally translated to p_H *via* eqn (3). Fig. 9 shows calculated carrier concentration dependence of PF at 800 K. An optimal carrier concentration of approximately 2.2×10^{21} cm^{-3} is obtained. The sample $x = 1.8$ seems to reach the highest electrical performance of the Te-doped Mo$_3$Sb$_7$ system with the acoustic phonon scattering assumption. The other Te-doped samples also fit the theoretical curve very well. Although an accurate prediction should utilize the much more complicated band structure calculations, all data are consistent with the SPB model, which is the simplest way to determine the trend of the electrical properties. Thus, in this paper, we simply show the reasonable trend of the electrical
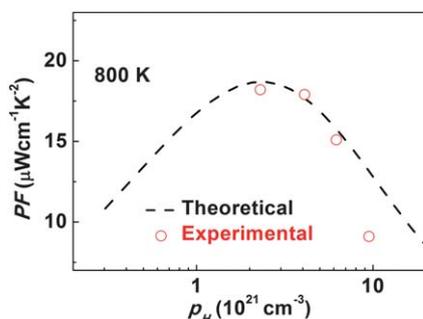
performance in a Te-doped Mo$_3$Sb$_7$ system with SPB model. Further improvement due to the non-parabolic nature of the bands needs to be developed with further band structure calculations.

Thermal properties

The high-temperature total thermal conductivity (κ) and lattice thermal conductivity (κ_L) were plotted in Fig. 10 and Fig. 11, respectively. Here, the lattice thermal conductivity was obtained by subtracting the electronic component (κ_e) from the total thermal conductivity, where the κ_e is determined by the Wiedemann-Franz law ($\kappa_e = L_0\sigma T$). The Lorenz number L_0 is frequently a debatable parameter when using the Wiedemann-Franz law, especially at the high temperature region. In this paper, the Lorenz number L_0 is calculated by employing a SPB model,

$$L_0 = -\frac{k_B^2}{e^2} \cdot \frac{(1+\lambda)(3+\lambda)F_\lambda(\eta)F_{2+\lambda}(\eta) - (2+\lambda)^2 F_{1+\lambda}(\eta)^2}{(1+\lambda)^2 F_\lambda(\eta)^2} \qquad (8)$$

Here, the carrier mobility is assumed to be limited by the mixed scattering by alloy and an acoustic phonon ($\lambda = 0$) and the reduced Fermi energy η is obtained as a function of temperature from the experimental Seebeck coefficients using eqn (5). For the high-temperature region, the values of L_0 obtained from eqn (8) are accurate where the single band model applies. The L_0 values decrease with increasing temperature for all samples as shown in Fig. 12. These L_0 values were adopted to calculate the lattice thermal conductivity in Fig. 11.

The thermal conductivity of the Mo$_3$Sb$_7$ exhibits interesting behavior. Mo$_3$Sb$_7$ has the largest thermal conductivity of the Mo$_3$Sb$_{7-x}$Te$_x$ series measured within the whole temperature range and it also increases with increasing temperature, which is similar with most metals. However, the lattice thermal conductivity of Mo$_3$Sb$_7$ shows the smallest value among all the samples. Thus, large thermal conductivity mainly comes from the electrical part κ_e.

Furthermore, the lattice thermal conductivity increases with increasing Te-doping fraction, which is very different from normal alloys. Typically alloying produces point defect scattering and therefore reduction in the lattice thermal conductivity.[27–29] In order to show clearly, the room temperature lattice thermal conductivity is plotted in the inset of Fig. 11. The trend

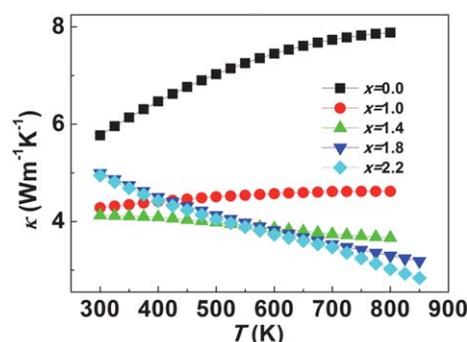**Fig. 9** Hole concentration dependence of the power factor PF at 800 K. The dashed line represents the theoretical curve and the dots are the experimental results.

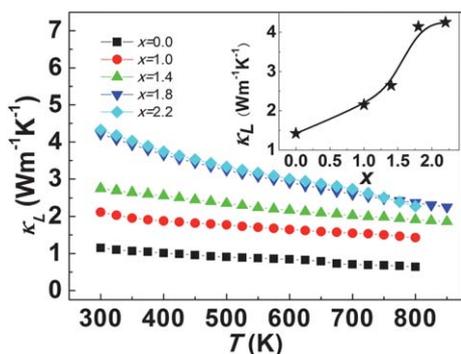**Fig. 10** Temperature dependence of the total thermal conductivity for Mo$_3$Sb$_{7-x}$Te$_x$.

Fig. 11 Temperature dependence of the lattice thermal conductivity for $Mo_3Sb_{7-x}Te_x$. The insert figure plots lattice thermal conductivity as a function of x at room temperature.

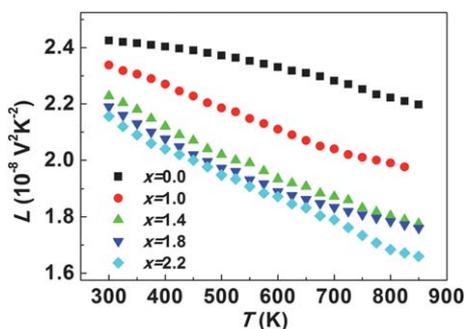**Fig. 12** Temperature dependence of the Lorenz number for $Mo_3Sb_{7-x}Te_x$.

in lattice thermal conductivity abruptly stops when the Te content reaches the solubility limit ($x \sim 1.8$) similar to the trends observed in the electrical properties. Clearly the disorder due to a point defect caused by doping can not explain the increase of the lattice thermal conductivity with doping. In fact, due to the similarity in mass and size of the Sb and Te elements, the doping should not cause severe mass and strain field fluctuation scattering. Thus, some other scattering mechanisms should be dominant instead of point defect scattering.

The effect of decreasing lattice thermal conductivity as electrical conductivity increases has been observed in other doped semiconductors. In $La_{3-x}Te_4$ this effect has been largely attributed to the softening of the lattice phonons due to screening of the ions or weakening of the bonds as free charge carriers are added and antibonding states filled (n-type) or bonding states depopulated (p-type).[30] Additionally, the electron–phonon interaction can contribute to phonon scattering and reduce lattice thermal conductivity.[31]

To distinguish these different mechanisms, we used Callaway's formalism to further investigate the thermal conductivity of the compounds.[32] Thermal conductivity due to the heat transport by phonons is given by

$$\kappa_L = \frac{k_B}{2\pi^2 v}\left(\frac{k_B T}{\hbar}\right)^3 \int_0^{\theta_D/T} \frac{\tau_C(y,T)y^4 e^y}{(e^y-1)^2} dy \qquad (9)$$

where $y = \hbar\omega/k_B T$, ω is the phonon frequency, $\hbar$ is the reduced Planck constant, θ_D is the Debye temperature, v is the velocity of

sound, and τ_C is a combined relaxation time. Usually, the phonon scattering relaxation rate τ_C^{-1} can be written as

$$\tau_C^{-1} = \tau_B^{-1} + \tau_{PD}^{-1} + \tau_U^{-1} + \tau_{ep}^{-1}$$
$$= \frac{v}{L} + A\omega^4 + B\omega^2 T\exp\left(-\frac{\theta_D}{3T}\right) + C\omega^2 \qquad (10)$$

where L is the grain size and the coefficients A, B, C are fitting parameters. The terms in eqn (10) represent grain boundary scattering (τ_B), point defect scattering (τ_{PD}), phonon-phonon Umklapp scattering (τ_U), and electron–phonon scattering (τ_{ep}), respectively. In the region where $T > \theta_D$ the quantity y in eqn (9) is small, and the integral simplifies to

$$\kappa_L = \frac{k_B}{2\pi^2 v}\left(\frac{k_B T}{\hbar}\right)^3 \int_0^{\theta_D/T} \tau_C y^2 dy \qquad (11)$$

Also, the exponential factor in the Umklapp relaxation time can be ignored for high T. At the high temperature region, the grain boundary term is often negligible.[33]

Often, the electron–phonon scattering is ignored at high temperatures as it is usually considered a low temperature effect. Even from eqn (10) we can find that the temperature-independent electron–phonon scattering, if it exists, will be overwhelmed by the Umklapp scattering effect, which becomes more dominant with increasing temperature.

So, we can model the data only with processes known to be present and ignore the electron–phonon interaction for now. Then the relaxation time can be expressed as

$$\tau_C^{-1} = \tau_{PD}^{-1} + \tau_U^{-1} = A\omega^4 + BT\omega^2 \qquad (12)$$

Eqn (11) and (12) can be further reduced by the method used by Ambegaokar,[34] to

$$\kappa_L \equiv W_L = W_{PD} + W_U, \text{ (this reduction requires } W_L \gg W_{PD})$$

where

$$W_{PD} = 4\pi^2 V_0 \theta_D \Gamma / hv^2$$

$$W_U = \pi vhBT/\theta_D k^2 \qquad (13)$$

V_0 is the average volume per atom in the crystal, and Γ is the point impurity scattering parameter.[35] Here, the W_{PD} of the $Mo_3Sb_{5.2}Te_{1.8}$ sample is calculated through eqn (13) and the value is $W_{PD} = 0.014$ mK W^{-1}, only 5% of the total thermal resistivity at room temperature due to the small mass and size difference between Te and Sb. Because $Mo_3Sb_{5.2}Te_{1.8}$ is the most heavily doped sample in this study, in principle, the other samples should have a lower W_{PD} value, which then should also be negligible as compared with the total W_L. Thus, for the sample $Mo_3Sb_{5.2}Te_{1.8}$, we assume that the high-temperature lattice thermal conductivity is dominated by the Umklapp scattering and ignore the point defect influence. Then, according to the expression of W_U in eqn (13), the maximum value of B_{max} is obtained.

The B parameter is a characteristic of the Umklapp process, which closely depends on the Debye temperature θ_D via the

This journal is © The Royal Society of Chemistry 2011

Energy Environ. Sci., 2011, **4**, 4086–4095 | 4091

relationship $B \sim h\gamma^2/2\pi m\theta_\mathrm{D}v^2$,[36] where γ is Grüneisen's constant and m is the average mass of a single atom. Also, because the velocity of sound is proportional to the Debye temperature, then the parameter B should be proportional to θ_D^{-3}. The Debye temperature is a very important parameter for the phonon-phonon interaction. In order to investigate the Debye temperature, the low-temperature heat capacity was studied. Fig. 13 shows the low-temperature specific-heat data (2–8 K), C_p/T, plotted as a function of T^2. The data were fitted using the relation

$$C_p = \alpha T + \beta T^3 \tag{14}$$

where αT the electronic contribution with α as the Sommerfeld constant and βT^3 as the lattice contribution. The values of α and β are listed in Table 2. The fitted parameter β can be used to calculate the Debye temperature through the formula

$$\theta_\mathrm{D} = (12\pi^4 NR/5\beta)^{1/3} \tag{15}$$

where N and R represent the number of the atoms in the compound formula and the gas constant, respectively. As shown in Table 2, the Debye temperature increases with increasing the Te doping fraction, which should result in decreased Umklapp scattering. Here, we used the calculated $B_{\max}$ value of $Mo_3Sb_{5.2}Te_{1.8}$ as well as the relationship of $B \sim \theta_\mathrm{D}^{-3}$ with the measured Debye temperatures to estimate the $B_{\max}$ values for the other samples. Thus, the maximum thermal resistivity from the Umklapp process is calculated through eqn (13) and compared to the total thermal resistivity from the experimental data. As shown in Fig. 14, the thermal resistivity from Umklapp scattering decreases with increasing Te doping fraction, which is attributed to the increased Debye temperature. From this point of view, low Debye temperature is beneficial for obtaining relatively high thermal resistivity or low thermal conductivity. However, the Umklapp scattering seems not enough to explain the total thermal resistivity of the samples, especially the ones with a relatively low Te doping fraction.

We now hypothesize that the other contribution of thermal resistivity may come from the electron–phonon scattering, which was temporarily ignored when making the analysis of eqn (12). Although the electron–phonon interaction is not so obvious or even negligible in many lightly doped semiconductors at high temperature, it may become much more important in heavily
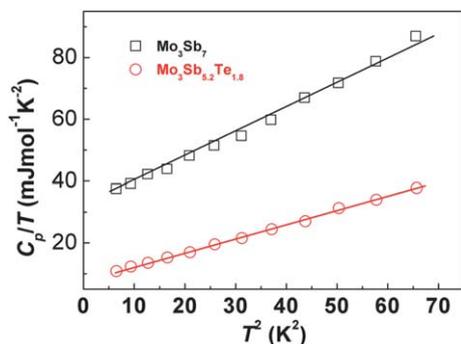
doped semiconductors or systems with high carrier concentrations, especially if those possess a large effective mass. Actually, the electron–phonon scattering behavior could be observed in some skutterudite systems when increasing the carrier concentration and this effect should be more obvious in systems with a large effective mass.[31,37] Here, the matrix compound Mo_3Sb_7 exhibits an extremely high carrier concentration of nearly 10^{22} cm^{-3} as well as a relatively large effective mass of $5m_e$. So it is reasonable to consider the electron–phonon interaction in such a "poor metal". Thus, the relaxation times should include the electron–phonon term and eqn (13) is modified to

$$\tau_C^{-1} = \tau_{PD}^{-1} + \tau_U^{-1} + \tau_{ep}^{-1} = A\omega^4 + (BT + C)\omega^2 \tag{16}$$

The thermal resistivity from electron–phonon scattering can be expressed as

$$W_{ep} = \pi vhC/\theta_\mathrm{D}k^2 \tag{17}$$

If we still ignore the point defect contribution, the total thermal resistivity is

$$W_L = W_U + W_{ep} = \frac{\pi vh}{\theta_D k^2}(BT + C) \tag{18}$$

By fitting the experimental W_L vs. T, the parameters B and C could be obtained. Fig. 15 shows the fitting result of both B and C, respectively. In Fig. 15a, the B parameter decreases with increasing Te doping fraction. The dashed line represents the calculated results using the B value from the sample $Mo_3Sb_{5.2}Te_{1.8}$ as well as the relationship of $B \sim \theta_D^{-3}$. The calculated results agree well with the fitting data, which means the relationship of $B \sim \theta_D^{-3}$ is satisfied remarkably well in the Te-doped Mo_3Sb_7 system and the decreased Umklapp scattering is partly responsible for the increased lattice thermal conductivity with Te-doping. Furthermore, the C parameter is also plotted in Fig. 15b with the dependence on carrier concentration. Here, the C can be written as [31,38]

$$C = \frac{4pm* v_e\lambda_e}{15dv^2} \tag{19}$$

where p is the carrier concentration in p-type material, v_e is the electron velocity that can be replaced by the Fermi velocity v_F.[31] λ_e is the mean free path of the electrons, and d is the mass density. We replace λ_e by $\lambda_e = v_e\tau_e = v_e\tau_0 E^{\lambda-1/2}$, where τ_e is the electron scattering relaxation time, E is the energy, λ is the scattering parameter, which is equal to 0 when the acoustic phonon dominates, and τ_0 is a constant. Here, we only consider the electron–phonon interaction for the relaxation time because the electron–phonon scattering dominates at high temperature. Also, we have the equation of

$$E = \frac{1}{2}m* v_F^2 \tag{20}$$

So the C parameter can be expressed as

$$C \propto \frac{2\tau_0 pE^{1/2}}{15dv^2} \tag{21}$$

According to the Boltzmann transport equation (eqn (3) and (4)) within the relaxation time approximation, the energy E has a relationship of $E \sim p^{2/3}$ with the carrier concentration, p.

Fig. 13 Low-temperature specific-heat C_p/T for Mo_3Te_7 and $Mo_3Sb_{5.2}Te_{1.8}$ as a function of T^2. The solid lines display the fittings for the data. The details of the fitting results are shown in Table 2.

Table 2 Fitting parameters α, β from low-temperature specific-heat analysis and calculated Debye temperature θ_D

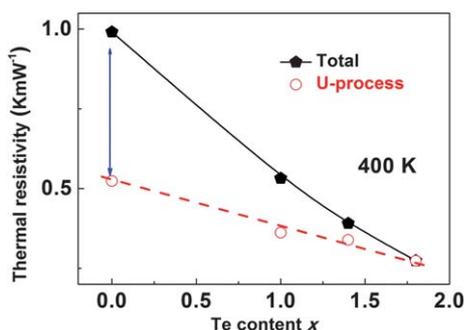| Nominal composition	α (mJ mol^{-1} K^{-2})	β (mJ mol^{-1} K^{-4})	θ_D (K)
Mo_3Sb_7	29.5	0.86	282
Mo_3Sb_6Te	15.2	0.60	319
$Mo_3Sb_{5.6}Te_{1.4}$	10.1	0.56	326
$Mo_3Sb_{5.2}Te_{1.8}$	7.6	0.46	350

Fig. 14 Thermal resistivity *vs.* Te content at 400 K. The solid dots represent the total thermal resistivity (experimental data). The hollow dots show the thermal resistivity from the Umklapp process calculated from the W_U of $Mo_3Sb_{5.2}Te_{1.8}$ and the relationship of $B \sim \theta_D^{-3}$. The dashed line is a linear guide to the eye.

Finally, the parameter C is proportional to $P^{4/3}$ if assuming the other parameters are constant or independent of carrier concentration. Although it is a very rough estimation, it does show that the electron–phonon interaction is sensitive to the carrier concentration. As shown in Fig. 15b, the parameter C fitting data follow the $p^{4/3}$ curve. Furthermore, a similar result and trend could also be obtained at different temperatures. We used the fitted parameter B in Fig. 15a to calculate the thermal resistivity W_{ep} for different temperatures from eqn (18). The result, shown in Fig. 16, shows that thermal resistivity is very close at different temperatures, indicating this part of contribution is temperature-independent. Also, it increases with increasing the carrier concentration, following the rough relationship of $p^{4/3}$, predicted above for the electron–phonon interaction behavior. Thus, it is reasonable to conclude that the electron–phonon scattering is another important aspect for influencing the thermal conductivity in the Mo_3Sb_7 system. Actually, a similar sharp carrier concentration dependence of the electron–phonon thermal resistivity was observed in another system,[39] supporting our assertion that the electron–phonon scattering for the phonons is very sensitive to the carrier concentration. On the other hand, it is also acceptable to ignore this contribution in the lightly doped materials, whose carrier concentration is always an order of magnitude smaller than Mo_3Sb_7, because the electron–phonon interaction is much more than an order of magnitude smaller. In addition, we note that the electron–phonon interaction of the sample $Mo_3Sb_{5.2}Te_{1.8}$ whose carrier concentration is still at a very high level compared with the ordinary thermoelectric materials, is relatively small, so the electron–phonon interaction may not be significantly contributing to the high zT. Nevertheless Mo_3Sb_7 appears to be an
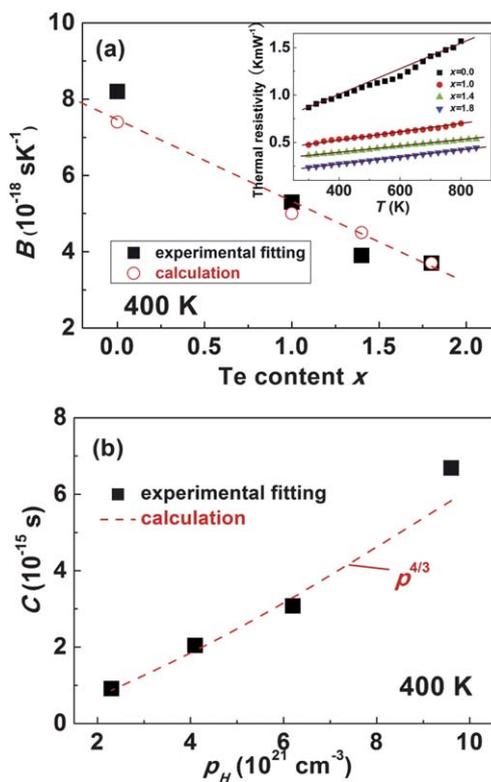

Fig. 15 (a) The B parameter of the Umklapp process *vs.* Te content. The solid dots are the fitting results using eqn (18) and the hollow dots represent the calculation result according to the relationship of $B \sim \theta_D^3$ (the data from the $Mo_3Sb_{5.2}Te_{1.8}$ sample are the starting point). The dashed line is a linear guide to the eye. The inset figure is the fitting result of the thermal resistivity. (b) Carrier concentration dependence of the C parameter. The solid dots are the fitting results and the dashed line represents the relationship of $p_H^{4/3}$.

excellent system, to explore the influence of electron–phonon scattering on the lattice thermal conductivity.

Although we could not quantify every part that contributes to the thermal conductivity accurately, a rough estimation of the high-temperature lattice thermal conductivity does show that the combination of depressed Umklapp scattering and electron–phonon scattering is the main reason for the increased lattice thermal conductivity after Te doping.

Umklapp scattering is temperature dependent and will be dominant at high temperature, while the electron–phonon scattering is temperature independent, which may account for the abnormal lattice thermal conductivity at low temperature. If so, as a high-temperature TE material based on Mo_3Sb_7, any further work should be focused on tuning the electrical performance
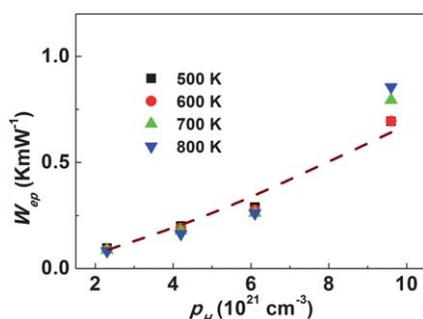
Fig. 16 Carrier concentration dependence of thermal resistivity from electron–phonon interaction at different temperature. The dashed line represents the relationship of $p_H{}^{4/3}$. Here, thermal resistivity is proportional to the C parameter according to eqn (17). So thermal resistivity shows the trend of the C parameter under different temperature and carrier concentration.

without disturbing the chemical bonding and maintaining a relatively high Umklapp scattering process to the phonons.

The figure of merit zT

The high temperature figure of merit zT was calculated and shown in Fig. 17. As a comparison, the figure of merit zT of SiGe (ref. 5) is also plotted in Fig. 17. The zT value of $Mo_3Sb_{7-x}Te_x$ increases with increasing Te content. The highest zT value reaches about 0.51 at 850 K and can be extrapolated to be about 0.8 at 1000 K for the sample $x = 1.8$. This is a very promising value, even higher than the SiGe system, for high-temperature p-type TE application.

Using the model for thermal conductivity as we described above, combined with the power factor of Fig. 9, results in an estimated zT peak of 0.48 at 800 K. As shown in Fig. 18, the optimized zT peak shifts to the lower carrier concentration region of around 1.1×10^{21} cm^{-3} compared to the power factor result in Fig. 9. Furthermore, if the Umklapp process could remain unchanged for all compounds with different carrier concentration, the zT will reach a higher value and the optimized zT peak may be located at lower carrier concentration. This work indicates that further improvement of the thermoelectric performance of the Mo_3Sb_7 system may be realized on the n-type doping of Mo atoms with some proper elements.[40]
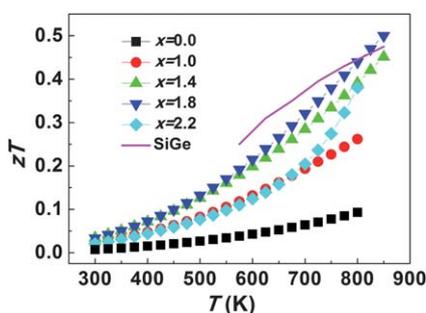

Fig. 17 Temperature dependence of the dimensionless figure of merit zT for $Mo_3Sb_{7-x}Te_x$. The solid line shows the figure of merit zT for SiGe from ref. 5.
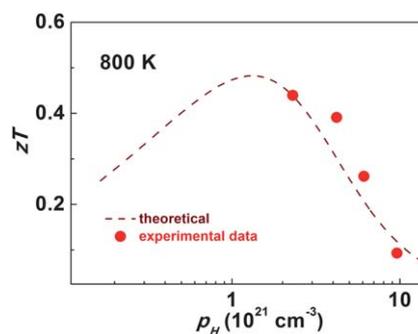

Fig. 18 Carrier concentration dependence of zT at 800 K. The solid dots are the experimental data and the dashed line represents the predicted zT curve using a single parabolic band model and the acoustic phonon scattering assumption. The lattice thermal conductivity was obtained from the simple model in this paper (see Thermal properties section).

4. Conclusions

$Mo_3Sb_{7-x}Te_x$ with $0 \leq x \leq 2.2$ was synthesized and subsequently characterized. The maximum Te/Sb substitution fraction is around $x = 1.8$. All samples exhibit metallic behavior with p-type conducting properties. The substitution of Te for Sb donates electrons, reducing the p-type doping and effectively optimizes the hole concentration, which results in improved thermoelectric properties. The optimal carrier concentration is around 2.2×10^{21} cm^{-3} based on the classic single parabolic band model and can be realized in $x = 1.8$ sample, which shows the highest zT of 0.51 at 850 K. From the analysis of high temperature thermal conductivity we conclude that the decreased Umklapp process and the electron–phonon interaction result in an increased lattice thermal conductivity after Te doping. It also gives us an inspiration that the electron–phonon scattering may play an important role in reducing the lattice thermal conductivity of heavily doped compounds with extremely high carrier concentration.

Acknowledgements

References

1 *CRC Handbook of Thermoelectrics*, ed. D. M. Rowe, CRC, Boca Raton, 1995.
2 F. J. DiSalvo., *Science*, 1999, **285**, 703.
3 T. M. Tritt, (ed.) *Recent Trends in Thermoelectric Materials Research* (Academic, San Diego, 2001).
4 G. Chen, M. S. Dresselhaus, G. Dresselhaus, J. P. Fleurial and T. Caillat, *Int. Mater. Rev.*, 2003, **48**, 45.
5 G. J. Snyder and E. S. Toberer, *Nat. Mater.*, 2008, **7**, 105.
6 H. J. Goldsmid, *Thermoelectric Refrigeration* (Temple Press Books Ltd, London, 1964).
7 A. J. Minnich, M. S. Dresselhaus, Z. F. Ren and G. Chen, *Energy Environ. Sci.*, 2009, **2**, 466.
8 J. J. Shen, T. J. Zhu, X. B. Zhao, S. N. Zhang, S. H. Yang and Z. Z. Yin, *Energy Environ. Sci.*, 2010, **3**, 1519.
9 J. Baxter, Z. X. bian, G. Chen, D. Danielson, M. S. Dresselhaus, A. G. Fedorov, T. S. Fisher, C. W. Jones, E. Maginn, U. Kortshagen, A. Manthiram, A. Nozik, D. R. Rolison, T. Sands, L. Shi, D. Sholl and Y. Y. Wu, *Energy Environ. Sci.*, 2009, **2**, 559.

10 E. S. Toberer, A. F. May and G. J. Snyder, *Chem. Mater.*, 2010, **22**, 624.

11 Y. Z. Pei, X. Y. Shi, A. LaLonde, H. Wang, L. D. Chen and G. J. Snyder, *Nature*, 2011, **473**, 66.

12 A. F. May, J. P. Fleurial and G. J. Snyder, *Phys. Rev. B: Condens. Matter Mater. Phys.*, 2008, **78**, 125205.

13 A. F. May, E. Flage-Larsen and G. J. Snyder, *Phys. Rev. B: Condens. Matter Mater. Phys.*, 2010, **81**, 125205.

14 S. R. Brown, E. S. Toberer, T. Ikeda, C. A. Cox, F. Gascoin, S. M. Kauzlarich and G. J. Snyder, *Chem. Mater.*, 2008, **20**, 3412.

15 E. S. Toberer, C. A. Cox, S. R. Brown, T. Ikeda, A. F. May, S. M. Kauzlarich and G. J. Snyder, *Adv. Funct. Mater.*, 2008, **18**, 2795.

16 U. Häussermann, M. Elding-Ponten, C. Svensson and S. Lidin, *Chem.–Eur. J.*, 1998, **4**, 1007.

17 E. Dashjav, A. Szczepenowska and H. Kleinke, *J. Mater. Chem.*, 2002, **12**, 345.

18 F. Gascoin, J. Rasmussen and G. J. Snyder, *J. Alloys Compd.*, 2007, **427**, 324.

19 C. Candolfi, B. Lenoir, J. Leszczynski, A. Dauscher, J. Tobola, S. J. Clarke and R. I. Smith, *Inorg. Chem.*, 2009, **48**, 5216.

20 C. Candolfi, B. Lenoir, J. Leszczynski, A. Dauscher and E. Guilmeau, *J. Appl. Phys.*, 2009, **105**, 083701.

21 C. Candolfi, B. Lenoir, C. Chubilleau, A. Dauscher and E. Guilmeau, *J. Phys.: Condens. Matter*, 2010, **22**, 025801.

22 H. Q. Zhang, J. He, B. Zhang, Z. Su, T. M. Tritt, N. Soheilnia and H. Kleinke, *J. Electron. Mater.*, 2007, **36**, 727.

23 H. Xu, K. M. Kleinke, T. Holgate, H. Zhang, Z. Su, T. M. Tritt and H. Kleinke, *J. Appl. Phys.*, 2009, **105**, 053703.

24 C. Candolfi, B. Lenoir, A. Dauscher, J. Hejtmánek and J. Tobola, *Phys. Rev. B: Condens. Matter Mater. Phys.*, 2009, **79**, 235108.

25 C. Candolfi, B. Lenoir, A. Dauscher, E. Guilmeau, J. Hejtmánek, J. Tobola, B. Wiendlocha and S. Kaprzyk, *Phys. Rev. B: Condens. Matter Mater. Phys.*, 2009, **79**, 035114.

26 A. F. May, Eric S. Toberer, Ali Saramat and G. J. Snyder, *Phys. Rev. B: Condens. Matter Mater. Phys.*, 2009, **80**, 125205.

27 P. G. Klemens, *Proc. Phys. Soc., London, Sect. A*, 1955, **68**, 1113.

28 J. Callaway and H. C. Vonbaeyer, *Phys. Rev.*, 1960, **120**, 1149.

29 B. Abeles, *Phys. Rev.*, 1963, **131**, 1906.

30 O. Delaire, A. F. May, M. A. McGuire, W. D. Porter, M. S. Lucas, M. B. Stone, D. L. Abernathy, V. A. Ravi, S. A. Firdosy and G. J. Snyder, *Phys. Rev. B: Condens. Matter Mater. Phys.*, 2009, **80**, 184302.

31 J. Yang, D. T. Morelli, G. P. Meisner, W. Chen, J. S. Dyck and C. Uher, *Phys. Rev. B: Condens. Matter*, 2002, **65**, 094115.

32 J. Callaway, *Phys. Rev.*, 1959, **113**, 1046.

33 C. J. Glassbrenner and G. A. Slack, *Phys. Rev.*, 1964, **134**, A1058.

34 V. Ambegaokar, *Phys. Rev.*, 1959, **114**, 488.

35 G. A. Slack, *Phys. Rev.*, 1962, **126**, 427.

36 G. A. Slack and S. Galginaitis, *Phys. Rev.*, 1964, **133**, A253.

37 H. Anno, K. Matsubara, Y. Notohara, T. Sakakibara and H. Tashiro, *J. Appl. Phys.*, 1999, **86**, 3780.

38 A. B. Pippard, *Philos. Mag.*, 1955, **46**, 1104.

39 A. M. Poujade and H. J. Albany, *Phys. Rev.*, 1969, **182**, 802.

40 D. Parker, M. H. Du and D. J. Singh, *Phys. Rev. B.*, 2011, **83**, 245111.